Biophysical Journal, Volume *119*

Supplemental Information

Amoeboid Swimming Is Propelled by Molecular Paddling in Lymphocytes

Laurene Aoun, Alexander Farutin, Nicolas Garcia-Seyda, Paulin Nègre, Mohd Suhail Rizvi, Sham Tlili, Solene Song, Xuan Luo, Martine Biarnes-Pelicot, Rémi Galland, Jean-Baptiste Sibarita, Alphée Michelot, Claire Hivroz, Salima Rafai, Marie-Pierre Valignat, Chaouqi Misbah, and Olivier Theodoly

Movies

Movie 1 : **From Crawling to Swimming in the vicinity of a substrate.** (Left) Crawling on adhering ICAM-1-treated substrate. (Right) Swimming on Pluronic© F127 treated surface. First sequence, 20x bright field transmission microscopy, then 63x bright field transmission microscopy and finally x63 reflected interference contrast microscopy.

Movie 2 : **3D imaging of primary human effector T lymphocyte swimming in spinning disk microscopy.** Videomicroscopy sequence of swimming T lymphocytes stained with CMFDA (5-chloromethylfluorescein diacetate) on Pluronic© F127 treated surface for 14 min 40 sec with a time lapse every 20 s and stack of 10 slices taken every 1 µm. Some unpolarized cells do not swim. The arrow points a polarized and swimming cell that crosses the whole field of view. Scale bars in µm indicated on axis, magnification: 63X.

Movie 3 : **Immediate transition between crawling and swimming**. Migration on alternative 40 µm wide stripes of adherent ICAM-1 and non-adherent Pluronic© F127 prepared by LIMAP[31]. Superimposition of fluorescent image (ICAM-1, red), bright filed transmission image (greyscale) and reflection interference contrast microscopy image (bright green corresponds to cells adhesion fingerprints) taken at 63x.

Movie 4 : **Swimming in bulk suspension.** Movie of two cells suspended in a medium of matched density using a microscope tilted by 90°and a flow chamber oriented vertically for sideway observations.

Movie 5 : **Correlation of swimming direction with cell polarization axis**. T lymphocytes swimming on Pluronic© F127 treated surface imaged in bright field at 10x of primary human effector. The red bars direction represents the instant tangent to trajectory, and their norm is proportional to the ratio between instant speed and maximal speed reached by the cells. The yellow bars direction represents the orientation of the ellipse having the same second-moment as the segmented cell, and their norm scales with the value of the ellipse eccentricity, as (exp(ecc)-1)/(exp(1)-1), where ecc is the eccentricity of the ellipse which varies between 0 and 1. (For more details see Suppl. Mat. Figure S 3 and corresponding paragraph).

Movie 6 : **Role of actomyosin network in swimming motion.** Movies in bright field at 63x of primary human effector T lymphocytes swimming on Pluronic© F127 treated surface in the presence of actin inhibitors: control, 50 µM Blebbistatin, 0.05 µM Latrunculin or 100 µM CK666. Scale bar 20 µm.

Movie 7 : **3D live imaging by so-SPIM of the actin cytoskeleton of swimming primary human effector T lymphocyte**. Video microscopy movie of RFP-Lifeact transfected cell, showing lamellar-protrusion forming with random orientation in cell front and travelling backwards at around 10 $\mu m.min^{-1}$.

Movie 8 : **Live bright field imaging of swimming primary human effector T lymphocytes showing protrusion retrograde motion and nucleus forward squeezing through constricted rings**. Bright field videomicroscopy at 63x of primary human effector T lymphocytes swimming on Pluronic© F127 treated surface. Scale bars 10 µm.

Movie 9 : **Swimming of a cell by the motion of two blebs on the cell surface.** The color here represents the mean curvature of the cell surface.

Movie 10 : **Lymphocytes swimming with perturbation of cell body deformation**. Bright field videomicroscopy at 63x of primary human effector T lymphocytes swimming on Pluronic© F127 treated surface in pure medium (left) and in a medium diluted with water at 50% (right). Osmotic

stress cancels the deformations of cell body by swelling but cell speed is 8 μm.min^{-1} like for control cells.

Movie 11 : **Cell membrane retrograde flow revealed by attached beads**. Bright field videomicroscopy of ICAM-coated beads travelling from front to back on the cell membrane of swimming T-cells in HBSS control media, 50 μM Blebbistatin, 0.05 μM Latrunculin, or 100 μM CK666.

Movie 12 : **Numerical simulation of swimming by retrograde flow.** Cell shape is extracted from experiments. The swimming is shown in the laboratory frame. Color code on the surface represents the production/consumption of the cortex material. Small spheres are fictitious tracers moving with the cortex velocity. Transmission coefficient θ = 1.

Movie 13 **: Evidence that actin bound proteins LFA-1 are advected backwards at cell membrane whereas non actin bound proteins MHC-1 are diffusive**. TIRF-FRAP experiments on primary human effector T-cell (Top left) transfected with a GFP-Actin by lentiviral infection, (Top right) stained with membrane lipidic marker DiO, (Bottom left) stained with antibody Mab24 that binds an actin-bound protein, the integrin LFA-1 in its high affinity state, and (Bottom right) stained with anti-HLA-ABC that binds the non-actin-bound MHC-1 type I proteins. Scale bars 5 μm.

Movie 14 : **Cytoskeleton retrograde flow**. TIRF imaging of a primary human effector T lymphocyte transfected with GFP-Actin and displaying backward travelling of clusters. Scale bar 5 μm.

Movie 15 : **Single cell evidence of average backward advection for actin-bound LFA-1 and average absence of motion for non-actin-bound MHC-1.** TIRF images after FRAP bleaching of a line pattern revealing actin-bound activated LFA-1 in its high affinity state (left) and non-actin-bound MHC-1 (right). Scale bar 5 μm.

Movie 16 : **Evidence that advected proteins LFA-1 are recycled at the cell front by internal vesicular transport whereas diffusive proteins MHC-1 are not**. TIRF-FRAP experiments on primary human effector T-cell (Right) stained with antibody Mab24 that binds the actin-bound proteins LFA-1 in high affinity state, and (Left) stained with anti-HLA-ABC that binds the non-actin-bound proteins MHC-1. The cell front is frapped and fluorescence recovers only from the front for LFA-1, in agreement with an internal vesicular recycling of integrins from back to front, and only from the rear for HLA, in accord with a surface diffusion mechanism.

Movie 17 : **Lymphocytes are motile when confined between non-adherent plates.** Movies in bright field at 20x of primary human effector T lymphocytes moving between two glass substrates patterned with an adherent zone covered with ICAM-1 (left) and an anti-adhesive zone (right). The round shapes correspond to 100 μm diameter glass pillars that sustain the structure.

Movie 18 : **Lymphocytes are motile when confined in tubes.** Movies in bright field at 63x of a primary human effector T lymphocytes moving in a non-adherent microfluidic channel of cross-section 4 x 4 μm^2.

Supplementary information on swimming speed experiments

Cells are non-adherent on Pluronics-treated substrates

Interference contrast microsocopy was used to assess the adhesion states of lymphocytes on 2D substrates. In Figure S 1 RICM images were inverted, thresholded and colored in green. The green zones correspond therefore to the adherent contact zone of cells. The projected area of cells was determined from the contour of the cells imaged in bright field. Cell adhesion was then quantified for each cell by the ratio of adherent area versus the projected area. Most polarized cells were adherent on ICAM-1 substrates with a mean adhesion in projected area of 40 ± 15 %. In contrast, 100 % of polarized cells had an adhesion in projected area lower than 5 % on Pluronics substrates, which corresponded to background level and therefore no detectable adhesion.

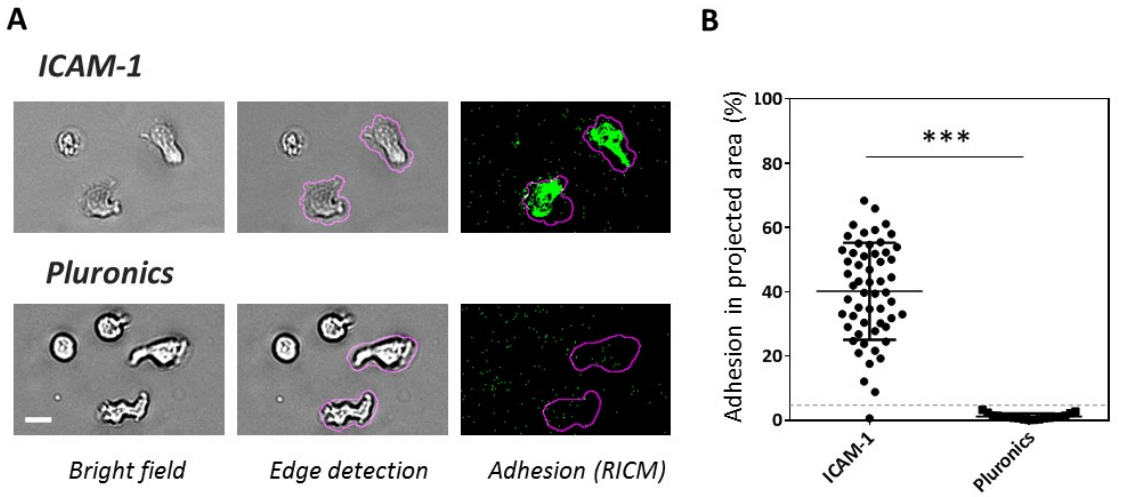

Figure S 1 : **RICM quantification of cell adherence on substrates coated with ICAM-1 and Pluronics: (A)** Microscopy data on ICAM-1 (top) and Pluronics (bottom) treated substrates. **Left-** Bright field images. **Middle-** Cell outlines determined using ilastik. **Right-** Superposition of cell contours with inverted (white signal on dark background) RICM images, application of rolling ball algorithm (to flatten the image with 10pix kernel size), and thresholding above background levels (with same threshold for all images). **(B)** Quantification of the adhesion area (determined by RICM signal) in the projected area of each cell (determined by the cell contours). Each point corresponds to one cell. Nexperiments = 3, Ncells = 57 for ICAM-1, Ncells = 21 for Pluronics, ***P < 0.001 (two-tailed Student's t test).

Experimental swimming speeds in suspension are independent of distance to a wall

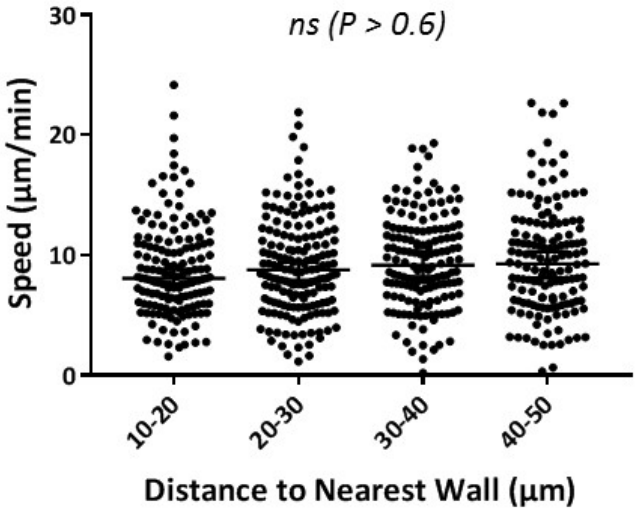

Figure S 2 : Swimming speed of active cells in suspension measured using the set-up of Figure 3 as a function of the distance to the nearest wall. Each data point corresponds to one step motion of a swimming cell for an interval of 30 s. Nexperiments = 10, Ncells = 66 Nsteps > 620. *P < 0.05, **P < 0.001, ***P < 0.001, with respect to distance to nearest wall, one way ANOVA with post Turkey's multiple test.

Propulsion of non-adherent cells is directed along polarization axis and toward lamellipod

The angular difference between the direction of polarization of cells migrating on an non adherent substrate and their instant displacement direction was determined on bright field images at magnification x20 (Movie 5). Binary images were analyzed in Matlab using the built-in *regionprops* function providing the orientation of the ellipse having the same second-moment as the segmented cell, and its eccentricity defined as the ratio between the foci of the ellipse and its major axis length. The direction of instant displacement was calculated on 30s time intervals. The angle calculated between cell orientation and direction of instant displacement was defined as the acute angle between both lines, taken positively. Thus this angle reached minimal value 0° when both directions are parallel or anti-parallel, and maximal value 90° when they are orthogonal. In order to select active cells, the histograms took into account all instant configurations of cell shape orientation and displacement direction provided that they reach a certain level of polarization and motility (eccentricity>0.5, instant speed>5um/mn). In order to have a negative control without correlations between cell shape and cell motion direction, we analyzed image sequences of fixed cells and released the constraints on polarization and motility levels. For active cells, either in normal medium or with blebbistatin treatment, histograms of Figure S 3 show a maximum probability for cell motion

collinear to cell polarization, whereas for fixed cells there is no preferential orientation of motion (The spikes at selected angles such as 45°are artefacts due to pixellisation that favor angle calculated with finite number of pixels). Altogether, this analysis shows cell activity and cell polarization are linked to the process of non-adherent migration and swimming, and that cells always progress in the direction of their lamellipod. Interestingly, cells treated with blebbistatin display a stronger correlation between motion directivity and polarization axis (SD equals 19.7 for blebbistatin versus 27.1 for control). This suggests that the contractility and the subsequent strong shape deformations of control cells are a source of stochasticity that hinders directionality.

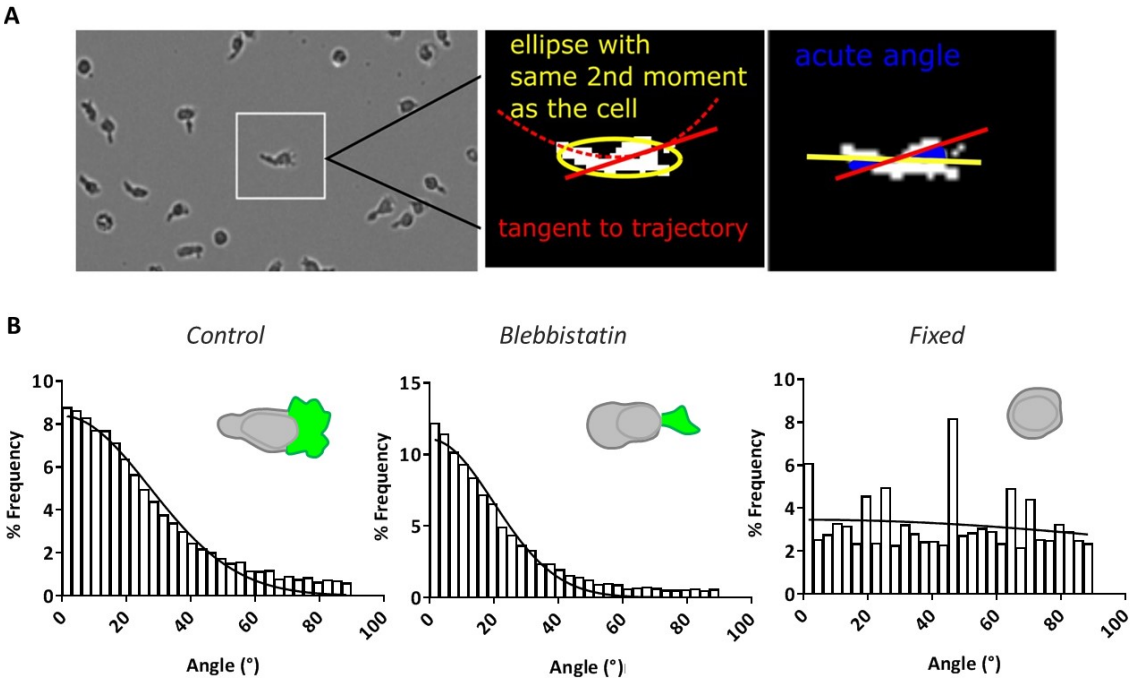

Figure S 3 : **Propulsion of non-adherent cells correlates with polarization. (A)** *Rationale of the analysis to extract direction of polarization and of instant displacement for individual cells.* ***Left-*** *Image source taken at magnification x10.* ***Middle-*** *Direction of instant displacement (red) is the tangent of the cell trajectory (between 3 points taken every 30 s), and direction of polarization (yellow) is the main axis of the ellipse corresponding to the second moment of cell contour.* ***Right-*** *The angle between direction of polarization and displacement is taken as the acute angle between their axis of orientation. (***B)** *Frequency of motion events versus the angle between cell polarization and direction of instant displacement for active cells in normal medium (**left**), active cells treated by Nlebbistatin (**middle**), and fixed cells (**right**). The drawings are schematics of cells morphology with cell body (grey) and lamellipod (green). The solid lines correspond to fits by a single Gaussian centered*

to a mean of zero. The standard deviation of the Gaussian is SD = 27.1° for control cells, SD = 19.7° for Blebbistatin treated cells and SD = 131.1° for fixed cells. Ncell = 226, 860, 92 and Nevents = 12411, 13646 and 12531 for respectively control, Blebbistatin and fixed cells. The histograms are normalized with respect to the total number of events. (See also Movie 5)

Experimental swimming speeds are independent of medium viscosity increase up to 100 times

Hydrodynamic interactions between an amoeboid lymphocyte and a fluid are sufficient to promote momentum transfer. In order to test how the viscosity of the medium influences the efficiency of cell-fluid coupling, we performed swimming experiments in culture medium supplemented with dextran of molecular weight 2,000 kDa to increase its viscosity to 10 and 100 times. Viscosity of solutions were measured on a Bohlin Gemini 150 rheometer equipped with cone-plate geometry (cone angle 20° , diameter 60 mm) at T=22°C (Figure S 4 –A). A control of the effect of osmotic pressure was performed with dextrose solution. Figure S 4 –B displays the histogram of cells speeds versus viscosities and osmotic pressure. The data in control medium and medium with dextrose are fitted with a double Gaussian, the Gaussian with lower mean speed corresponding to inactive and diffusing cells, the Gaussian with higher mean speed corresponding to active and swimming cells. The data in medium of increased viscosities were fitted by a single Gaussian because the inactive cells had a very low apparent mean speed and were sorted out by our tracking protocol. Figure S 4-C shows that apparent mean speed of inert and diffusing objects are indeed below 0.5 μm/min. The statistical analysis of speed for active cells (Figure S 4-D) shows that osmotic pressure had no significant effect on swimming speed within the range tested for viscosity measurements. For a viscosity increase by 10x, we observed a decrease of speed by 25 % that was statistically significant. However, this tendency of speed decrease with viscosity was not confirmed by a further increase of viscosity by 100x, for which the speed is found statistically similar as for the control. These observations support therefore the idea that viscosity plays no determinant role in propulsion speed, which is consistent with predictions of the model for swimming propelled by cell membrane retrograde flow or by protrusions.

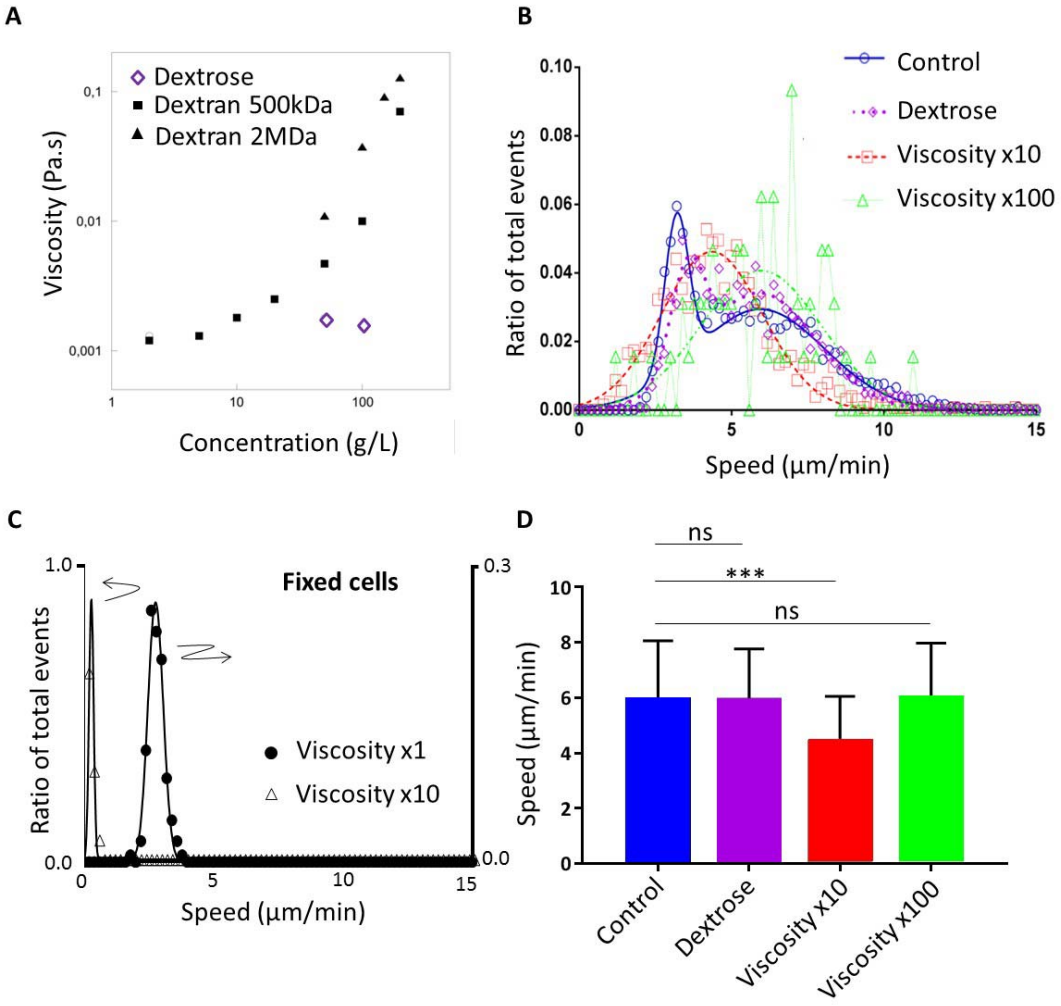

Figure S 4 : **Cell speed is independent of the medium viscosity. (A)** Viscosity of Dextran and dextrose solutions in HBSS versus concentration. **(B)** Histogram of raw curvilinear speed for cells in normal medium and medium with viscosity increased 10 x (Dextran 2,000 kDa at 50g/L) and 100 x (Dextran 2,000 kDa at 150g/L), and osmotic control condition (Dextrose 16g/L). Lines correspond to fit by a double Gaussian for normal medium and Dextrose and by a single Gaussian for medium of increased viscosity (10x and 100x). **(C)** Histogram of raw curvilinear speed for fixed cells in normal medium (filled dots) and in medium of viscosity x10, Dextran 2,000 kDa at 50g/L (Hollow triangles). **(D)** Average speed and standard deviation of active cells determined by the Gaussian fit of higher mean speed for normal medium and dextrose and by the single Gaussian for medium of increased viscosity. Ncells = 4342 (HBSS), 1262 (Dextran 50 $g.L^{-1}$), 64 (Dextran 150 $g.L^{-1}$), 1449 (Dextrose),), 139 (Fixed viscosity x1), 30 (Fixed viscosity x10); Nexperiments = 5 (HBSS), 3 (Dextran 50 $g.L^{-1}$), 3 (Dextran 150 $g.L^{-1}$), 2 (Dextrose), 2 (Fixed viscosity 1x), 2 (Fixed viscosity 10x). *P < 0.05, **P < 0.001, ***P < 0.001 with respect to control, one way ANOVA with post Turkey's multiple test.

Supplementary Table

Table 1 : Swimming speed versus the effects of cell fixation, medium viscosity change and actin inhibitors addition. The table reports the raw swimming speed estimated by averaging the instant curvilinear speeds between two positions of cell mass centre separated by 30s for each cell. Average raw speeds of active and passive cells as well as fraction of active cells extracted from the fit of the speeds histograms by a double Gaussian (Figure 2**Error! Reference source not found.**-B). Speed errors correspond to standard deviation. Cell number correspond to the number of cells considered for each experimental condition.

	Active cells		**Passive cells**	
Condition	**($\mu m.min^{-1}$)**	**Fraction**	**($\mu m.min^{-1}$)**	**Number of cells**
HBSS-CTRL	5.9 ± 2.1	78%	3.2 ± 0.4	4342
Blebbistatin	4.3 ± 1.1	45%	3.1 ± 0.4	2353
CK666	4.4 ± 0.8	21%	3.2 ± 0.4	5582
Latrunculin	4.2 ± 0.5	20%	3.3 ± 0.4	2255
Bleb. + Lat.	5.0 ± 0.3	2%	3.4 ± 0.3	403
HBSS-PFA	-	-	2.8 ± 0.3	139
Viscosity 10x	4.4 ± 1.6	NA	-	1262
Viscosity 100x	6.0 ± 2	NA	-	64
Dextrose	5.9 ± 1.8	80%	3.6 ± 0.6	1449
Visco 10x-PFA	-	-	0.27 ± 0.09	30
ICAM-1	14.6 ± 7.5	-	-	503

Supplemental information on swimming mechanism

Cell diffusion and persistent swimming: Model

We model the motion of the cells as a combination of deterministic swimming and random noise. The swimming velocity $v_s = v_s p$ is assumed to have a constant absolute value but the orientation vector p can vary in time. The random noise here consists of translational diffusion with diffusion coefficient D_t and rotational diffusion with angular diffusion coefficient D_r. This noise accounts both for thermal fluctuations and for the active dynamics of the cell. Since cells are swimming close to a wall, the dynamics of orientation p and position r of the swimmer are effectively two-dimensional. The model described above belongs to a broad class of persistent random walk problems, which have enjoyed a lot of attention in the literature[1] . We therefore give here only a brief overview of the solution process and the final expression of the mean square displacement of the cell as a function of time and the model parameters.

Cell diffusion and persistent swimming: Solution

We first calculate the correlation $\langle p(t_0) \cdot p(t) \rangle$. The probability density function $\psi(p,t)$ for the swimmer to have orientation p at time t satisfies the following equation:

Equation 1 $$\dot{\psi}(p,t) = D_r \nabla_p^2 \psi(p,t).$$

where $\nabla_p \equiv (I - p \otimes p) \cdot \partial_p$ is the gradient operator on a unit circle representing possible orientations of p, and I is the identity matrix. The right hand side of Equation 1 expresses the angular diffusion process. If $p(t_0) = p_0$, the initial condition for Equation 1 is

Equation 2 $$\psi(p,t_0) = \delta_p(p - p_0),$$

where δ_p is the Dirac function. Equation 1 is solved by expanding $\psi(p,t)$ in Fourier harmonics of p, which represents the eigenfunctions of the Laplace operator ∇_p^2:

Equation 3 $$\psi(p,t) = 1 + \psi_i(t) p_i + \psi_{ij}(t) p_i p_j + \ldots,$$

where $\psi_{ij}(t)$ and so on are symmetric and traceless. The quantity of interest here is $\psi_i(t) = 2\langle p_i(t) \rangle$. Substituting Equation 3 into Equation 1 yields $\psi_i(t) = \psi_i(t_0) exp[D_r(t_0 - t)]$ for $t \geq t_0$, resulting in

Equation 4 $$\langle p(t_0) \cdot p(t) \rangle = p(t_0) \cdot \langle p(t) \rangle = e^{-D_r|t-t_0|}.$$

The displacement due to persistent motion is calculated by integrating Equation 4:

Equation 5

$$\partial_t \langle [r(t) - r(t_0)]^2 \rangle = 2\langle v_s(t) \cdot [r(t) - r(t_0)] \rangle = 2 \int dt' \langle v_s(t) \cdot v_s(t') \rangle = 2v_s^2 \frac{1 - e^{-D_r|t-t_0|}}{D_r}.$$

Integrating Equation 5 and adding the contribution of the translational diffusion yields

Equation 6 $$\langle [r(t) - r(t_0)]^2 \rangle = \frac{2v_s^2}{D_r} \left(|t - t_0| + \frac{e^{-D_r|t-t_0|} - 1}{D_r} \right) + 4D_t|t - t_0|.$$

Equation 6 reduces to Equation 1 for $tD_r \ll 1$.

Model of swimming by blebs

In order to simulate the bleb-driven swimming of the cells, we model the cell as an elastic capsule, to which active forces are applied, while maintaining the zero net force and torque conditions (Figure S 5). The application of the active force density concentrated in small regions of the cell surface results in the formation of bleb-like protrusions. Further, the location at which the active forces are applied is moved with a prescribed velocity v_{bleb} along the surface of the cell. In addition to the magnitude of the active force and the bleb velocity, the life-time of the blebs, T_{bleb}, is also an important parameter that describes the duration for which the active force is applied. This application of time dependent active force leads to formation and movement of the blebs along the cell surface. The shape and size of the blebs depends on the material properties of the cell, small bending stiffness, leading to larger and more protrusive blebs.

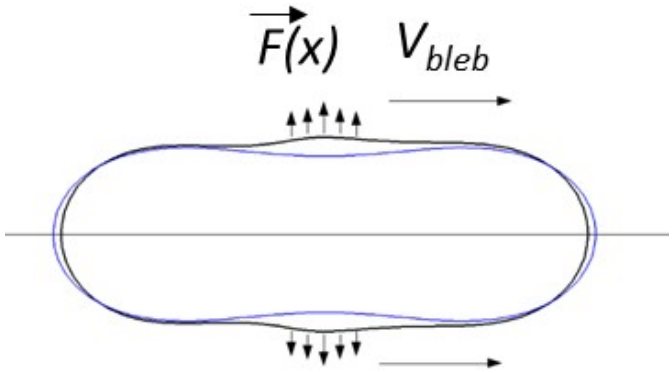

Figure S 5 : Schematic of a swimming cell by protrusive blebs. Blue and black contours are the initial and deformed configurations of the cell, respectively.

The configuration of the cell during the course of a bleb formation and motion is shown in Figure S 6 , and the maximum size of the blebs for different values of active force amplitudes is shown in Figure S 7.

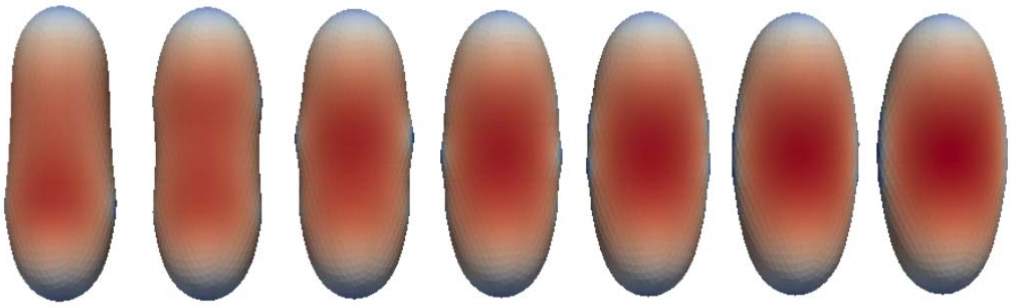

Figure S 6 : Configuration of the cells with a single pair of blebs at different time points. Progression of time is from left to right.

The swimming velocity is then obtained by solving the hydrodynamic problem in fluids inside and outside the cell, as described below and the velocity of the cell by the motion of a single pair of blebs is shown in Figure S 7-B. For all the simulations $v_{bleb}$was fixed at 0.02 and force amplitude *F* was varied. The plot shows that in bleb-driven swimming, the cell velocity $v_{cell} < 10^{-3} v_{bleb}$. Furthermore, the dependence of the swimming velocity on the force amplitude is $v \propto F^2$.

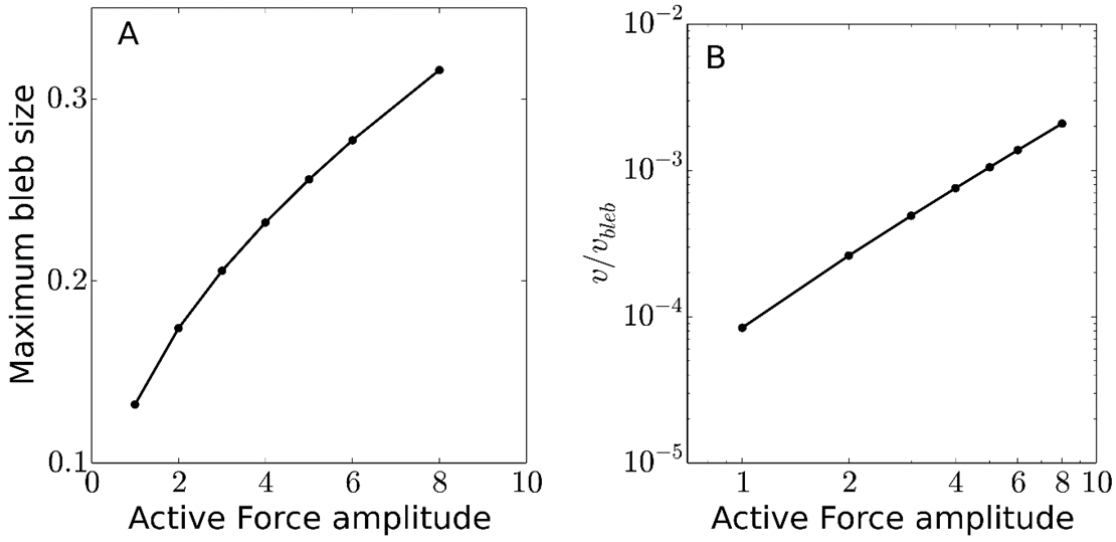

Figure S 7 : **(A)** Maximum size of the blebs for different values of active force amplitudes (see Figure S 5). **(B)** Dependence of average cell velocity $v_{cell} < 10^{-3} v_{bleb}$ on the active force amplitude. Here the bleb velocity relative to the cell centre has been kept fixed at $v_{bleb} = 0.02$.

Quantification by wavelet transform of experimental protrusion propagation modes

We tracked the cell contours of migrating cells image at magnification x60 in three conditions: (i) the "control condition", in normal medium, (ii) the " water condition" in a medium including 50% of

water, and (iii) the "blebbistatin condition", in a medium with a concentration of 50µM of Blebbistatin.

From the cell contour to cell edge to cell center distance kymographs

The cell contours were detected with the Ilastik software and the contour points exported in Matlab for further analysis. To reconstruct the contours with an homogeneous sampling around the cell perimeter, we used elliptic Fourier analysis with the "plot_fourier_approx.m" matlab function[2] to obtain a smooth contour of the cells. We used 50 modes for the reconstruction and N = 2000 points of sampling along the contour (Figure S 8-A). We then resampled a number of N = 500 points along the contour spaced by an equal curvilinear distance ds = cell perimeter/N. We calculated the distance R to each of these points to the cell barycenter (defined as the average position of all the points inside the cell contour) (Figure S 8-B). As cells from different conditions can have different average radii (the Blebbistatin condition cells are significantly smaller than the control cells), we computed the kymographs of the relative radius defined as $R \Big/ < R >_{time}^{space}$ with $< R >_{time}^{space}$ the cell average radius averaged in time and around the cell contour. The kymograph of the relative radius (with the position along the contour in the y axis and the time in the x axis) showed discontinuities that reflected potential rotations of the cell (Figure S 8-C,left). We removed these discontinuities by calculating the best shift maximizing the correlation coefficient between two consecutive kymograph columns and iteratively permuted the columns by a circular shift corresponding to the shift maximizing correlation between neighboring columns (this is equivalent to aligning consecutive images of the cell to remove its rotations). After aligning the kymograph, we shifted it circularly in order to have the lamelippodia at its center and the uropod at its two extremities (Figure S 8-C, right).

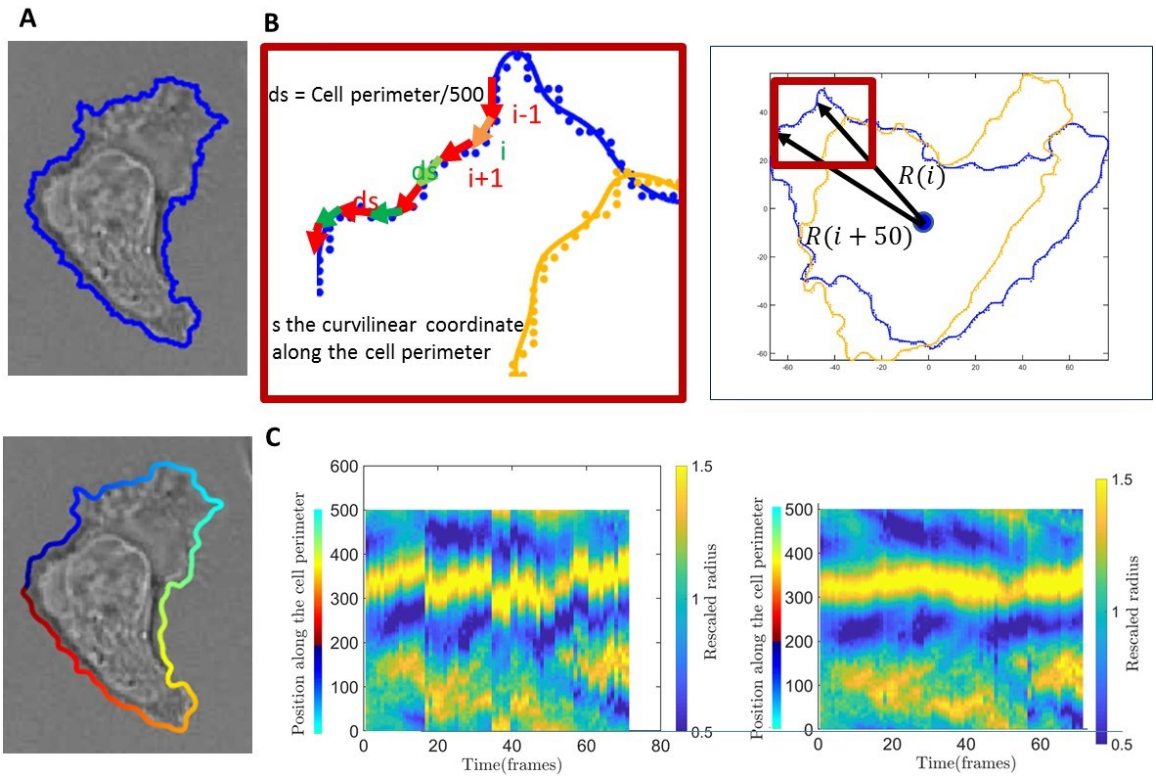

Figure S 8: Contour fluctuation analysis with Elliptic Fourier analysis. **(A) Top-** Raw cell contour extracting using Ilastik. **Bottom-** Contour from elliptic Fourier reconstruction. **(B)** Analysis of the cell edge-cell center distance, R, variations along the cell perimeter. Homogeneous sampling of step ds along the curve. **(C)** Kymographs of rescaled cell edge-cell distance before (left) and after (right) rotation correction.

Comparing the relative amplitude of cell contours waves in different conditions with wavelet spectral analysis

To analyze the waves of deformation observed qualitatively on the cells timelapses, we separated the relative radius kymograph in two parts: (i) its constant profile around the contour averaged in time, defined as the time average of the relative radius $< R >_{time} / < R >_{time}^{space}$ (it corresponds to the stable modulations of cell shape due to the polarized cell geometry during migration, with a main protrusion at the front (lamellipodia) and another one at the back (uropod)) (ii) its time varying part defined as $(R - < R >_{time}) / < R >_{time}^{space}$, which corresponds to the contour time fluctuations depending on space. We identified waves patterns in the corresponding kymograph, which can be mapped to the waves of deformation observed on the cell contours. To quantify these waves velocities and amplitude and to compare them between different cells and conditions, we then performed a 2D wavelet analysis of the kymographs using the 2D Morlet wavelet transform with the

matlab cwtft2.m function (Figure S 9). As all kymographs did not have the same temporal extension (total time between 70s and 160s) and temporal sampling (every 2 or 5s), we linearly interpolated all the kymographs at a sampling rate of 1 frame/s and we cropped big kymographs in two small kymographs of 70s in order to avoid any artefact in the wavelet analysis due to differences in kymographs size and sampling frequencies. As we analyzed the wave patterns in two dimensions, in order that the waves appear with reasonable angles in 2D, we subsampled by linear interpolation the kymograph in the y axis (the contour position axis), and we performed the wavelet analysis with kymographs of a fixed size of N = 68 points in the space dimension and N = 70 points in the time dimension. To obtain the wavelet spectrogram of each kymograph, we represent the magnitudes of the 2-D CWT coefficients (using the L1 norm convention) for angles between 0 and 180 degrees and scales between 8 and 60 (the scales correspond here to the periods observed in the 2D kymographs and the angles to their orientation, as any periodic pattern in the kymograph can be described by its period and its angle.) Although different cells in each condition displayed some variability, striking features appeared both on the kymographs and on the wavelet spectrograms. In the control condition, waves appeared on the spectrogram with angles close to 60 and 120 degrees and scales close to a value of 35, which corresponds to deformation waves propagating from the lamellipodia to the uropod at an average speed around a half cell perimeter/30s, or 10-20 µm/min (Figure 5-D). These waves can be identified strongly in the control and water condition. They can sometimes be identified in the blebbistatin condition but in an attenuated version and in many cases not. To quantify this feature, we computed the ensemble averaged spectrograms between all individual spectrograms in a same condition, to compare the average spectrogram for each condition Figure 5-E). We find a much lower amplitude in the blebbistatin case than in the control and water for all modes. On the main mode identified above as the waves of deformation mode, we observed a factor of 2 on the coefficients amplitude between the control and the blebbistatin, which is proportional to the average kymograph amplitude signal.

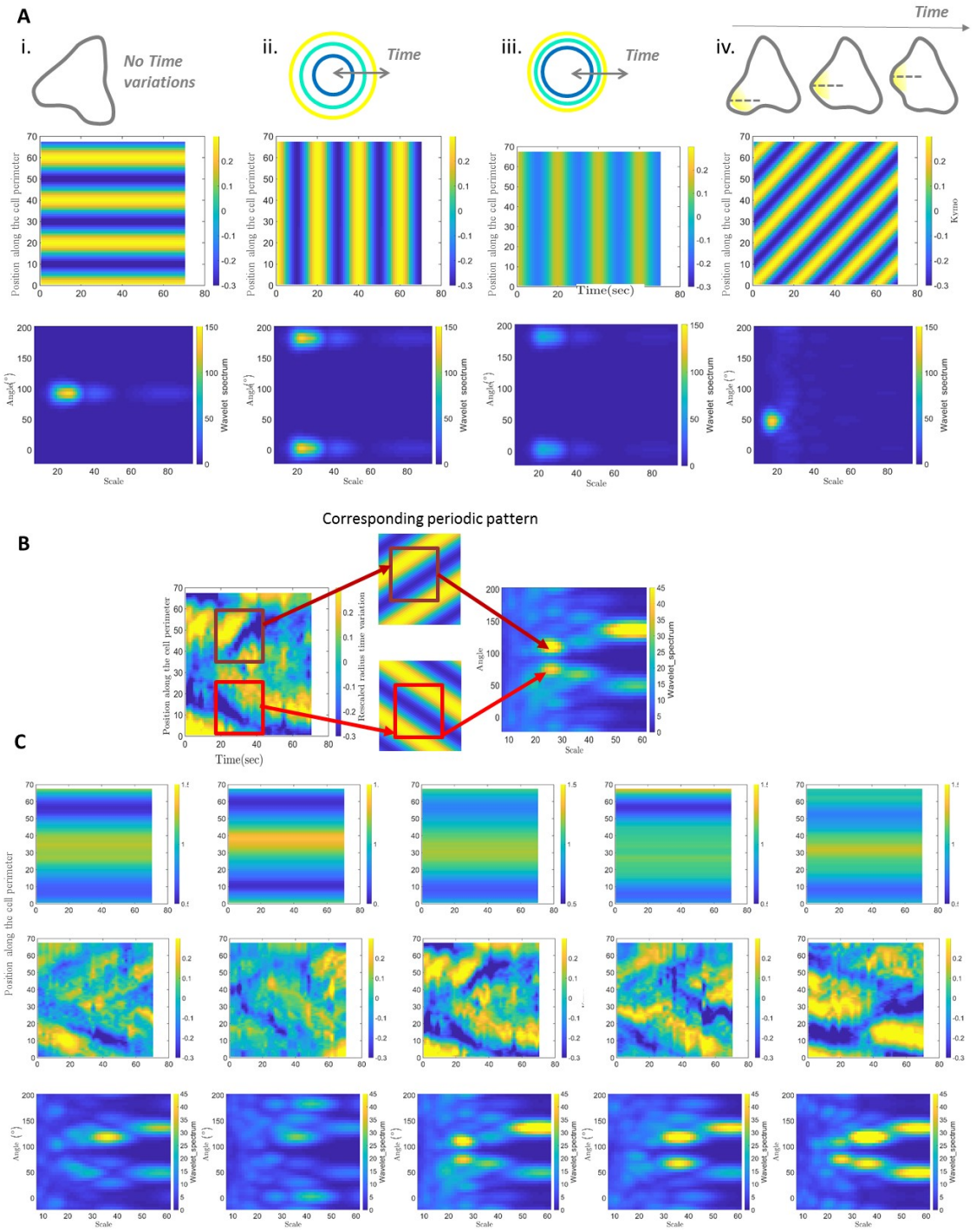

Figure S 9: Analysis with wavelets of the kymographs of cells contours. **(A)** Kymograph and wavelet spectra corresponding to ideal cases of i- a cell with irregular shape without time variations; ii and iii. a circular cell with periodic time variations of size. Amplitude in wavelet spectra reflects amplitudes of deformations; iv. cell with protrusions propagating backwards on the starboard side. **(B)** Identification in a kymograph of a cell contours (left) of the periodic patterns (middle) corresponding to a mode in the wavelet spectrum (right) of the kymograph. **(C)** Examples of time-averaged kymographs (top), corresponding kymograph with time-average contribution subtracted (middle), and corresponding wavelet spectrum (Bottom) for control cells.

Extension of the model of swimming by blebs to **multiple blebs with various size and coherence**

We have investigated further the evolution of the swimming speed in the presence of multiple protrusions (Figure S 10). We considered as an extreme limit the idealized situation where blebs move very coherently such that they form rings traveling along the surface from one pole to the other.

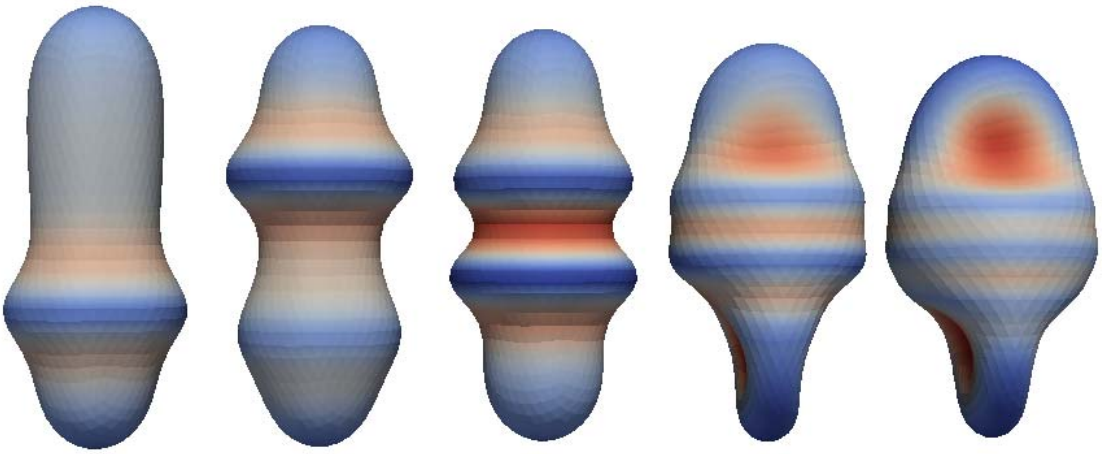

Figure S 10 : Cell shape at an instant for different number of blebs. The left most cell has only one pair of bleb at any time, the second cell has two pairs, and so on. The surface colour demonstrates the mean curvature.

The increase of their number leads to an increase of swimming speed until a value slightly less than 0.1 the retrograde flow and then drops as their number increase (Figure S 11). Note that blebs in the form of rings were never observed, meaning that locomotion caused by small waves traveling along the surface is unlikely, since the implied swimming speed would be even smaller.

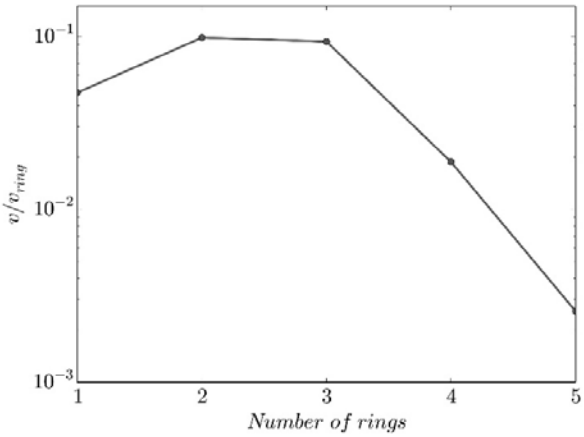

Figure S 11 : Normalized cell speed versus number of rings.

Model of swimming by membrane retrograde flow: Actin cortex flow

Actin polymerization expands the cortex in the front region of the cell, whereas myosin-induced contractility and actin depolymerization consume the cortex in the rear region of the cell. Between these regions, the actin moves from front to back along the cell membrane. An overpressure of the cortex at cell front due to actin accumulation and an underpressure at cell rear due to myosin-induced contraction can both contribute to forces driving the retrograde flow of the cortex. We thus model the driving force as the pressure gradient along the cell surface, $\nabla^S P$, where *P* is the pressure field and ∇^S is the surface gradient operator. This gradient implies a net cortex flow field $v_a(r)$ which, in a simple approximation, can be taken locally proportional to the driving force:

Equation 7 $$v_a(r) = -\mu\nabla^S P(r)$$

Where μ is a mobility coefficient. Here we assume that the shape is fixed so that the flow is tangential to the surface in the reference frame commoving with the cell. By choosing an appropriate pressure field, Equation 7 can be proven to be exact for any axisymmetric flow (see below). It is interesting to note that Equation 7 is identical to the Darcy law, valid in a porous medium or a Hele-Shaw flow. The cortex region could be viewed as a thin layer, a curved Hele-Shaw geometry, hence Equation 7 can be inferred from classical hydrodynamics. Equation 7 is closed by the mass conservation equation:

Equation 8 $$\nabla^S . v_a(r) = \psi_p(r) - \psi_d(r)$$

Here we express the change of the local 2D concentration of actin (per cortex area) due to the advection by the flow (the left hand side) through the local rate polymerization $\psi_p(r)$ (source) and the local rate of depolymerization $\psi_d(r)$ (sink). $\psi_p(r)$ and $\psi_d(r)$ are zero everywhere except in a small domain localized in the front and rear regions of the cell, respectively. Substituting Equation 7 into Equation 8 gives an equation for *P* which can be solved. Once *P* is determined the actin flow field $v_a(r)$ can be obtained from Equation 7.

Model of swimming by membrane retrograde flow: actin flow in ***an axisymmetric case***

The purpose is to show that for axisymmetric cells Equation 7 holds automatically. The cell shape and the actin velocity can be parametrized in cylindrical coordinates as

Equation 9 $$r(s,\varphi) = \big(\rho(s)cos(\varphi), \rho(s)sin(\varphi), z(s)\big),$$

Equation 10 $$v_a(s,\varphi) = v_a(s)\partial_s r(s,\varphi)$$

where s is the arclength measured from the front pole of the cell, φ is the polar angle, $\rho(s)$ and $z(s)$ are shape functions, and $\partial_s r(s,\varphi)$ is the tangent vector along the meridian. The properties of s are such that $|\partial_s r(s,\varphi)| = 1$. Equation 7 can be easily verified if we define $P(s,\varphi)$ as

Equation 11 $$P(s,\varphi) = -\frac{1}{\mu}\int v_a\,(s')ds'$$

Model of swimming by membrane retrograde flow: ***Exact solution for a spherical swimmer***

The actin flow can be obtained explicitly for a spherical cell having a point source of actin $\psi_p(r) = 2Rv_0\delta(r - r_N)$ at the North Pole r_N and a point sink $\psi_d(r) = 2Rv_0\delta(r - r_s)$ at the South Pole r_S. Here *R* is the sphere radius and v_0 is a constant having a dimension of velocity that turns out to be equal to the retrograde flow velocity at the equator in the cell frame. We present the solution in spherical coordinates. Defining the origin as the centre of the swimmer and the polar direction as source point of actin, we write the velocity at a point $(Rsin\theta cos\varphi, Rsin\theta sin\varphi, Rcos\theta)$ as

Equation 12 $$v(\theta,\varphi) = \Big(v_0\frac{cos\theta}{sin\theta}cos\varphi, v_0\frac{cos\theta}{sin\theta}sin\varphi, -v_0\Big),$$

where θ is the azimuth angle. The corresponding actin pressure is written as

Equation 13 $$P(\theta,\varphi) = \frac{v_0}{2\mu}ln\frac{1+cos\theta}{1-cos\theta}$$

The swimming velocity is then given by $v_s = \beta v_0$.

Flow outside the cell

Since the Reynolds number in the problem is extremely low, the flow v_f in the fluid outside the cell membrane satisfies the Stokes equations:

Equation 14 $$\eta_0\nabla^2 v_f - \nabla p = 0, \qquad \nabla\cdot v_f = 0,$$

where η_0 is the viscosity of the suspending medium. Equation 14 are solved together with the boundary conditions given by $v_f = 0$ at infinity and Equation 17 of the main text. The unknowns v_s and ω_s are solved for from conditions:

Equation 15 $$\int F\,dA = 0,$$

Equation 16 $$\int F \times r dA = 0,$$

where F is the surface force density applied locally by the fluid to the cell, dA is the area element and integrals are taken over the boundary of the cell membrane. Equation 15 and Equation 16 express that no external forces or torques act on the swimmer. The forces F can be expressed through the viscous stress tensor σ of the fluids

Equation 17 $$F_i = -\sigma_{ij} n_j, \quad \sigma_{ij} = \eta_0 \left(\partial_i v_{fj} + \partial_j v_{fi}\right) - p\delta_{ij},$$

where n is the outward normal to the boundary of the cell. It follows from the linearity of Equation 14 and Equation 2 of the main text that for any a, if v_f, v_s, ω_s, σ, F, and p represent a solution of the problem for a given cell shape, v_a and external fluid viscosity η_0, then v_f, v_s, ω_s, $a\sigma$, aF, and ap represent a solution of the problem for the same shape, v_a and external fluid viscosity $a\eta_0$. This implies that changing viscosity of the suspending medium does not affect the swimming velocity for the same velocity of the retrograde flow and the same transmission coefficient β. This result is consistent with experimental observations (cf. Suppl. Mat., Figure S 4 and "Experimental swimming speed are independent of medium viscosity increase up to 100 times").

Model of swimming by membrane retrograde flow: *Numerical method for any swimmer*

We parametrized the surface of the cell obtained in experiments by a triangular mesh. The Laplace equation for *P* (Equation 7 substituted in Equation 8) was solved by finding a stationary solution of a diffusion equation. The flow in the suspending fluid was solved for using the boundary integral formulation. The details of the numerical procedure and the validation are given in [3].

Vicinity of a wall is negligible

We have also solved the numerical problem for a swimmer near a solid wall. The no-slip boundary condition at the wall was imposed by taking a modified Green's function in the boundary integral formulation, as discussed in Pozrikidis C (1992)[4]. The same shape and retrograde flow field were taken as in the unconfined case. The orientation of the wall was chosen consistently with the experiment but the position was varied in order to scan different gaps between the cell and the wall. The resulting dependence of the swimming velocity (assuming $\beta = 1$) is shown in Supplemental Figure S9.

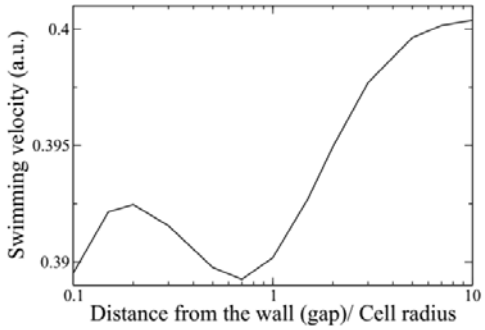

Figure S 12 : Calculated swimming velocity of cell powered by cell membrane treadmilling versus the distance of the cell to the wall normalised by the cell size. The presence of the wall influences only marginally cell speed between 0.39 and 0.4.

Quantification of LFA-1 and VLA-4 expression on effector T lymphocytes.

Quantification LFA-1 and VLA-4 number per cell was performed by quantitative cytometry (Figure S 13) and yielded an average number per cell of 25000 for LFA-1 and 15,000 for VLA-4.

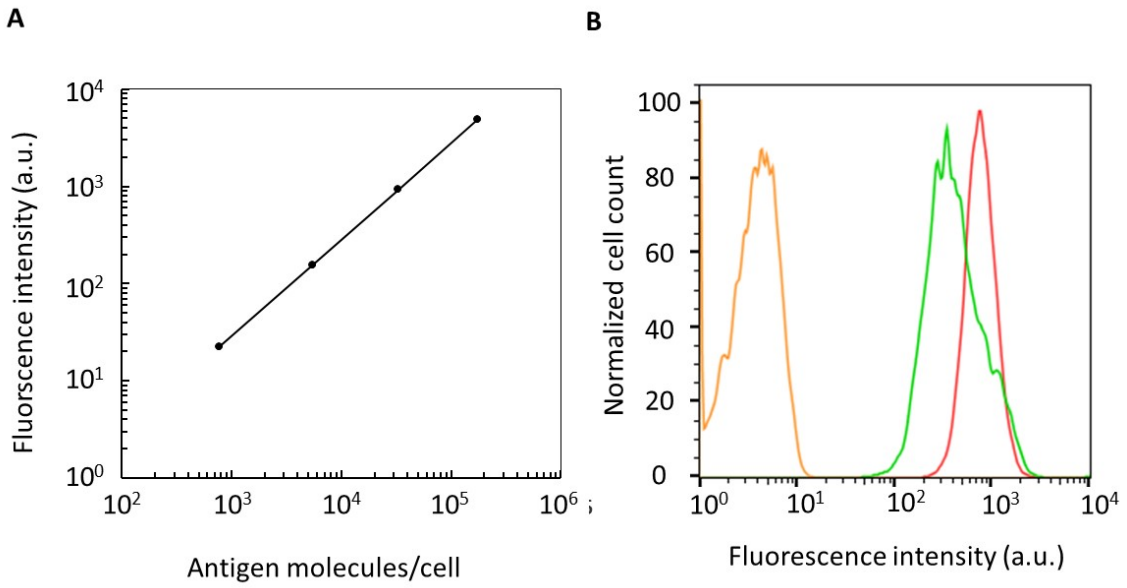

Figure S 13 : **(A)** Calibration curve with the secondary antibody and calibration beads (CellQuant calibrator kit, ref 7208, Biocytex). **(B)** Fluorescence histograms of T lymphocytes stained by indirect immunofluorescence with specific monoclonal antibodies CD49d (HP2/1) for VLA-4 (green) and CD11a (Hi111) for LFA-1 (red).

Model of swimming by membrane retrograde flow: ***Molecular paddling model***

The purpose of this section is to introduce a detailed model of the transfer of the cortex retrograde flow to the fluid surrounding the cell. The model is based on a mean-field approximation: we consider a region of a cell boundary that, on one hand, is large compared to the size of individual proteins, and, on the other hand, is sufficiently small compared to the cell scale. These assumptions allow us to consider the cell boundary to be flat and to represent all relevant quantities as a function of the distance from the cortex, averaging them over the two remaining coordinates. The freely diffuse and the cortex-bound proteins are thus modelled as a homogeneous porous medium with an effective viscous friction with the fluid. A similar model was considered[5] for a flow of fluid inside a brush of polymers covering a wall and subject to an external flow. We therefore only list here the main ingredients of the solution and final results.

The following analysis is written in the reference frame comoving with the phospholipid bilayer. We consider the actin-bound proteins to move with the cortex velocity v_a, as suggested by our measurements showing that high affinity integrins LFA-1 are advected at a speed very close to the one of actin cortex (Figure 7-I), and we call v_p the speed of proteins not bound to actin. The exact numbers of advected and non advected proteins are however not known precisely. Finally, we

assume that the individual protein molecules interact only via hydrodynamic fields in the outside fluid, thus excluding short-range solid friction between them. The proteins also interact via hydrodynamic fields inside the bilayer. However, since the net velocity of the bilayer is zero in the chosen frame, this interaction would only result in a correlation of velocities in pairs of proteins located closely to each other. This would represent a higher-order effect in the concentration of cortex-bound proteins than the one considered here.

The protein brush can be modelled by the Brinkman equations[6], which can easily be motivated as follows. The fluid in the brush is to leading order function only of the coordinate z orthogonal to the cell membrane (since the brush thickness is small as compared to the cell size), and obeys the one-dimensional nonhomogeneous Stokes equation

Equation 18 $$\eta_0 \partial_{zz} v_{fx}(z) + f_x(z) = 0,$$

Where $f(z)$ is the volume-related force density applied by the brush on the fluid, given by

Equation 19 $$f_x(z) = \xi_i\big[v_a - v_{fx}(z)\big] + \xi_p\big[v_p - v_{fx}(z)\big],$$

where $\xi_i = \varphi_i^{2D}\,\zeta_i/V_i$ is the volume-averaged drag coefficient of actin-bound proteins (e.g. integrins LFA-1 in the experimental part) and $\xi_p = \varphi_p^{2D}\,\zeta_p/V_p$ is the volume-averaged drag coefficient of passively advected proteins (e.g. MHC-1 in the experimental part). Here φ^{2D} is the area fraction of corresponding proteins, ζ is the corresponding viscous drag coefficient, and V is the volume of the extramembrane part of the corresponding protein.

The velocity of the free proteins, v_p, is calculated by requiring the sum of drag forces applied by them on the fluid and the bilayer to be equal to zero, which gives a condition:

Equation 20 $$f_x^{bl} h^{bl} + \xi_p \int \big[v_p - v_{fx}(z')\big]\, dz' = 0,$$

where h is the thickness of the brush and h_{bl} is the thickness of the bilayer. The drag experienced by the freely advected protiens from the phospholipids of the bilayer f_x^{bl} is expressed as

Equation 21 $$f_x^{bl} = \xi_{bl} v_p,$$

where $\xi_{bl} = \varphi_p^{2D}\,\zeta_{bl}/V_{bl}$ is the volume-averaged drag coefficient inside the bilayer for passively advected proteins, ζ_{bl} is the corresponding Stokes drag coefficient for one protein, and V_{bl} is the volume of the protein part inside the bilayer. Note that the cortex-bound proteins experience drag inside the bilayer just as the passive ones do but their velocity is fully determined by the flow of the cortex, to which they are firmly attached.

Equation 18 and Equation 19 can be solved for v_{fx} as a function of v_a and v_p by using the two boundary conditions:

Equation 22 $$v_{fx}(0) = 0, \quad \text{and} \quad \partial_z v_{fx}(h) = 0.$$

Equation 20 and Equation 21 yield the expression of v_p as a function of v_a, and thus the full expression of the fluid velocity field as a function of drag coefficients, the membrane thickness and v_a. From this knowledge we determine β (which is the transmission coefficient of the cortex flow to the fluid at the brush surface, $z = h$). β is function of the drag coefficients and the viscosities. The explicit forms of β, v_p, and v_{fx} read

Equation 23 $$\beta = \frac{\xi_a v_a + \xi_p v_p}{\xi_a + \xi_p}\left[1 - \frac{2g}{1+g^2}\right],$$

Equation 24 $$v_p = \xi_p \xi_i v_a \frac{\lambda h\left(1+g^2\right)+1-g^2}{\xi_p^2(g^2-1)+\left(\xi_i \xi_p h + h_{bl}\xi_{bl}\left(\xi_i+\xi_p\right)\right)\lambda(1+g^2)},$$

Equation 25 $$v_{fx} = \frac{\xi_i v_a + \xi_p v_p}{\xi_i + \xi_p}\left[1 - \frac{e^{\lambda z}+g^2 e^{-\lambda z}}{1+g^2}\right],$$

where $\lambda^2 = \left(\xi_i + \xi_p\right)/\eta_0$ and $g = e^{\lambda h}$.

The Stokes drag coefficients of the proteins in the outer fluid are written as $\zeta = 6\pi R_h \eta_0 \approx 10^{-10}\, kg/s$, where R_h is the Stokes radius, which we take here as 6 nm for simplicity. The Stokes drag coefficient in bilayer can be estimated directly from the measurements of the diffusion coefficient D_t^{2D} of MHC-1 freely advected proteins : $\zeta_{bl} = k_B\, T/D_t^{2D} \approx 10^{-8}\, kg/s$. The thickness of the bilayer is taken as 8 nm. The brush thickness is taken as 20 nm, which we estimate from the length of integrins in activated state. The volume of the external part of the proteins is taken as $V_i = V_p = 4\,\pi R_h^3/3 \approx 900 nm^3$. The volume of the bilayer segment of the passively advected proteins is estimated as $V_{bl} = \pi R_h^2 h_{bl} \approx 900 nm^3$. Supplemental Figure S 14 shows the transmission coefficient β and $\beta_p = v_p/v_a$ as a function of the concentration φ_p^{2D}.

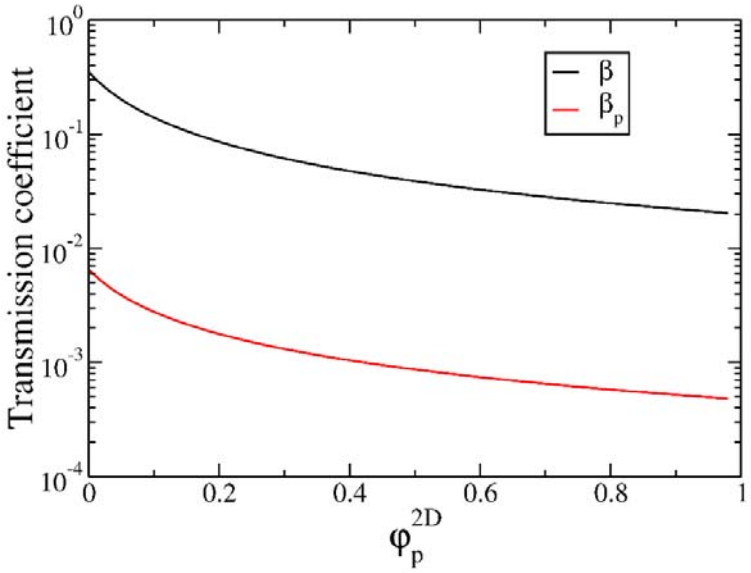

Figure S 14 : Transmission coefficients of the cortex flow to the fluid β (black curve) and to non advected proteins β_p (red curve) as a function of the concentration φ_p^{2D}, as given by Equation 23 and Equation 24. $R_h = 6nm, \eta_0 = 0.001Pa \cdot s,\ \ h = 20nm,\ \ \varphi_i^{2D} = 2\%, \zeta_{bl} = 10^{-8}\, kg/s$.

The analysis above was performed in the reference frame of the phospholipid bilayer. The experimental results do not allow us to establish whether a significant retrograde flow of the phospholipids is present in the reference frame of the cell membrane. Assuming the average local velocity of the phospholipids v_{bl} in the reference frame of the cell membrane is known, we can express the velocity fields in the reference frame of the swimmer membrane as $v_f + v_{bl}$ for fluid velocity, as$v_p + v_{bl}$ for freely diffusing proteins and as $v_a + v_{bl}$. The full expression for transmission coefficient is then written as $\beta(v_{bl}) = \beta(0) + \frac{v_{bl}}{v_a}\big(1 - \beta(0)\big)$, where $\beta(0)$ is given by Equation 26 and v_a is measured in the reference frame of the cell membrane. This shows that allowing for retrograde flow of the bilayer further increases the transmission coefficient.

BIBLIOGRAPHY

1. Saintillan, D. & Shelley, M. J. Active suspensions and their nonlinear models. *Comptes Rendus Phys.* **14**, 497–517 (2013).

2. Manurung, A. Elliptic fourier for shape analysis (https://www.mathworks.com/matlabcentral/fileexchange/32800-elliptic-fourier-for-shape-analysis). (2020).
3. Farutin, A., Biben, T. & Misbah, C. 3D numerical simulations of vesicle and inextensible capsule dynamics. *J. Comput. Phys.* **275**, 539–568 (2014).
4. Pozrikidis, C. Boundary Integral and Singularity Methods for Linearized Viscous Flow - doi:10.1017/CBO9780511624124. in (Cambridge University Press., 1992).
5. Kim, Y. W. *et al.* Nonlinear Response of Grafted Semiflexible Polymers in Shear Flow. *Macromolecules* **42**, 3650–3655 (2009).
6. Brinkman, H. C. A calculation of the viscous force exerted by a flowing fluid on a dense swarm of particles. *Flow Turbul. Combust.* **1**, 27 (1949).